Programmable Magnetic Microsystems

CNF Project Number: 900-00

Principal Investigator(s): Paul L. McEuen[1,2], Itai Cohen[1,2], Michael Brenner[3]

User(s): Tanner Pearson[4], Conrad Smart[5], Chrisy Xiyu Du[3], Hanyu Alice Zhang[4]

Affiliation(s): 1. Laboratory of Atomic and Solid State Physics, Cornell University; 2. Kavli Institute for Nanoscale Science, Cornell University; 3. School of Engineering and Applied Sciences, Harvard University; 4. School of Applied and Engineering Physics, Cornell University; 5. Department of Physics, Cornell University

Primary Source(s) of Research Funding: This work was supported by NSF grant DMR-1921567, Air Force Office of Scientific Research (AFSOR) multidisciplinary research program of the university research initiative grant FA2386-13-1-4118, Cornell Center for Materials Research (CCMR) through NSF MRSEC program (DMR-1719875), and the Kavli Institute at Cornell for Nanoscale Science. This work was performed in part at the Cornell NanoScale Science & Technology Facility (CNF), a member of the National Nanotechnology Coordinated Infrastructure NNCI, which is supported by the National Science Foundation (Grant NNCI-2025233)

Contact(s): plm23@cornell.edu, itai.cohen@cornell.edu, brenner@seas.harvard.edu, tgp34@cornell.edu, cs2239@cornell.edu, xiyudu@seas.harvard.edu, hz496@cornell.edu

Primary CNF Tools Used: Oxford FlexAL ALD, ASML DUV stepper, JEOL 6300, CVC e-beam evaporators, Oxford 81/82/100 etchers, PT770 and PT740 etchers, Anatech asher, Zeiss SEMs, Veeco atomic force microscope, Tencor P7 profilometer, Filmetrics UV, DISCO dicing saw, Heidelberg mask writer - DWL2000, AJA sputter deposition

Abstract:

We develop programmable microscopic systems based on nanomagnetic information. By taking advantage of magnetic shape anisotropy, we sequentially program the orientation of magnetic dipole moments on rigid panels. We can connect these panels with flexible glass hinges to develop actuatable structures capable of locomotion. Additionally, we can leave panels detached from each other and agitate them to demonstrate smart handshake self-assembly based on dipole-dipole interactions. These programmable systems have a diverse range of applications ranging from microrobotics to synthetic DNA assembly and replication.

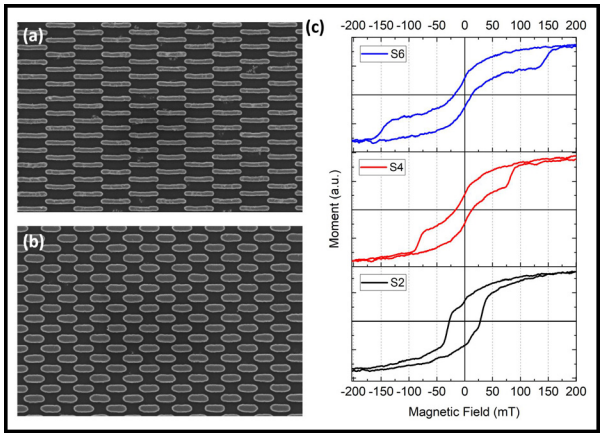

Figure 1: (a) SEM image of high AR nanomagnets. (b) SEM of low AR nanomagnets. (c) Magnetic hysteresis loops for different AR nanomagnets (S2 AR = 3, S4 AR = 5, S6 AR = 9). Width of hysteresis, and therefore coercive field, increases with increasing AR.

Summary of Research:

We create systems embedded with complex magnetic information by utilizing electron beam lithography (EBL) to fabricate single domain cobalt nanomagnets with varying aspect ratios (Figure 1a-b) [1]. The coercive fields of these nanomagnets and the orientations of their moments are intrinsically tied to shape anisotropy. Since magnetic moments prefer to be oriented along the long axis of a magnet, high aspect ratio (AR) magnets will exhibit higher coercive fields along their long axes than those with smaller aspect ratios. We tune the nanomagnet dimensions to achieve magnetic dipoles with coercive fields ranging from 30 mT to 140 mT (Figure 1c).

We sequentially program multiple magnetization directions by using two species of nanomagnets with disparate coercive fields [1]. With the long axis of the two species oriented along the same global axis, we apply a magnetic field greater than the coercivity of the high aspect ratio magnets to program all the magnets in one direction. We then use an opposing field with a magnitude between the coercivities of the two magnet species to reverse the orientation of the lower aspect ratio magnets. With an orthogonal pair of magnet species, we can achieve up to four discrete moment orientations ($\pm x$, $\pm y$). Superpositions of these moments provide additional orientations. We confirm dipole moment orientations with magnetic force microscopy (MFM) (Figure 2b).

We have previously shown that nanometer-thick glass deposited by atomic layer deposition (ALD) is an ideal material for flexible microsystems due to its incredibly low

bending stiffness [2]. By combining EBL and deep ultraviolet (DUV) lithography, we can integrate programmable nanomagnets onto rigid panels connected by flexible glass hinges to create a variety of actuatable devices. Here we show a device consisting of two panels, comprised of arrays of 800 nanomagnets with opposing moments, connected by two 5 nm thick glass hinges (Figure 2a-b). We can apply a uniform external field in z to torque both panels up or down, demonstrating the basic mountain-valley fold essential for microscopic origami and origami-inspired metamaterials.

Moreover, we can apply a combination of sinusoidal in-plane and out-of-plane fields to achieve a crawling motion akin to that of an inchworm (Figure 2c). Starting with both legs on the substrate, these fields continuously cycle through the following sequence of motions: the device tilts to its back leg, stretches the front leg forward, tilts to its front leg, pulls the back leg forward, and returns to its start position. In this way the device achieves net forward motion (Figure 2d). We can increase the frequency of this cyclic motion to achieve impressive crawling speeds of over a body length per second. Additionally, the phase and amplitudes of the in-plane field components can be modulated to achieve direction reversal and turning, respectively. This deceptively simple device illustrates how even a small amount of magnetic information can enable complex actuation dynamics necessary for robotic microsystems.

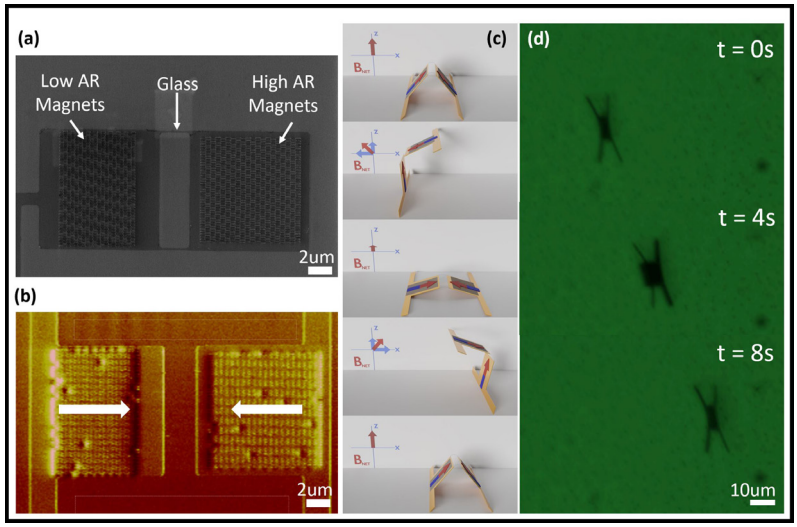

Figure 2: (a) SEM image of inchworm device. Glass hinges (dark grey) are each 250 nm × 2.5 µm. Panels are (10 µm)² and each consist of 800 magnets. (b) MFM image confirming the opposing net magnetic moments of each panel. (c) Cartoon illustrating stepping sequence of device. (d) Position over time of device cycled at 1 Hz, demonstrating net forward motion.

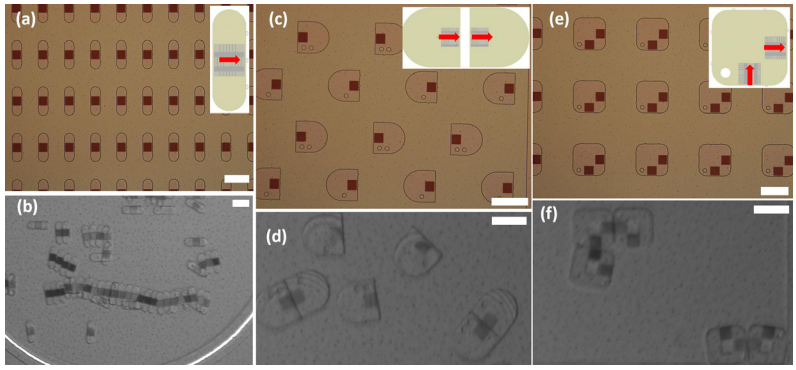

Figure 3: (a-b) Panels assembling into simple polymer chains. (c-d) Panels assembling into dimers. (e-f) Assembly of square panels with two dipole moments. Full assembly would yield 2 × 2 panel arrays. Insets show cartoons of panel magnetizations. Scale bars 30 µm.

We also use programmable nanomagnets to develop microscopic handshake systems capable of smart self-assembly (Figure 3) [3]. The fabrication process consists of embedding one or more nanomagnetic dipoles into thick, disconnected glass panels. When released from the substrate, panels are sonicated to facilitate lock-key binding of dipoles at the sides of complementary panels. With careful design of the panel geometry and magnetic dipole-dipole interactions, we can enable a wide range of well-defined assemblies. As the number of dipoles per panel increases, the lock-key binding becomes more specified, and more complex assemblies are possible. Moreover, these systems can be influenced by external magnetic fields at any point during or after the assembly process, providing a unique mechanism to manipulate assembled structures.

The possible applications for programmable nanomagnetic microsystems are immense. Magnetic panels connected by flexible glass hinges can be used to create mechanical and optical metamaterials and explore magnetically induced defects in those metamaterials. They can also be integrated into locomotive microrobots.

By eliminating the connective membranes between panels, we can further develop intelligent handshake systems governed by lock-key dipole-dipole interactions. These can be used to create assemblies that behave analogous to polymers and DNA.

References:

[1] J. Cui, T. Huang, Z. Luo, P. Testa, H. Gu, X. Chen, B. J. Nelson, L. J. Heyderman, Nature 2019, 575, 164.

[2] K. J. Dorsey, T. G. Pearson, E. Esposito, S. Russell, B. Bircan, Y. Han, M. Z. Miskin, D. A. Muller, I. Cohen, P. L. McEuen, Adv. Mater. 2019, 31, 1901944.

[3] R. Niu, C. X. Du, E. Esposito, J. Ng, M. P. Brenner, P. L. McEuen, I. Cohen, PNAS 2019, 116 (49), 24402.

Smart Microscopic Robots

CNF Project Number: 900-00

Principal Investigator(s): Paul L. McEuen[1,2], Itai Cohen[1,2], Alyosha C. Molnar[3], Marc Z. Miskin[4]

User(s): Michael F. Reynolds[1], Alejandro J. Cortese[1,3], Qingkun Liu[1], Wei Wang[1,5], Samantha Norris[1], Zhangqi Zheng[1], Sunwoo Lee[3]

Affiliation(s): 1. Laboratory of Atomic and Solid State Physics, Cornell University, Ithaca NY USA;
2. Kavli Institute at Cornell for Nanoscale Science, Cornell University, Ithaca NY USA;
3. Department of Electrical and Computer Engineering, Cornell University, Ithaca NY USA;
4. Department of Electrical and Systems Engineering, University of Pennsylvania, Philadelphia, PA, USA;
5. Sibley School of Mechanical and Aerospace Engineering, Cornell University, Ithaca NY USA

Primary Source(s) of Research Funding: CCMR, MURI, KIC, CNF REU Program (NSF grant NNCI-2025233)

Contact(s): plm23@cornell.edu, mfr74@cornell.edu

Primary CNF Tools Used: ABM contact aligner, Oxford 100 ICP dielectric etcher, Oxford 80 etchers, Oxford Cobra ICP etcher, AJA sputter deposition (1&2), Arradiance ALD Gemstar-6, Oxford ALD FlexAL, Oxford PECVD, Gamma automatic coat-develop tool, Xactic xenon difluoride etcher

Abstract:

Research on microscopic robots — robots a few hundred micrometers in size or smaller — has demonstrated a variety of approaches for locomotion and simple functions but has not produced "smart microscopic robots" that can perform complex tasks autonomously. Recently, our group has demonstrated the first smart microscopic robots by integrating microactuators with complementary metal oxide semiconductor (CMOS) electronics. These robots can actuate their legs independently and walk autonomously without any input of information. This work paves the way for smart microscopic robots that can sense and respond to their environment, receive commands, perform complex functions, and communicate with the outside world.

Summary of Research:

Figure 1 shows the first smart microscopic robot. An optical micrograph of one of these robots with labeled parts is shown in Figure 1A. Its body consists of photovoltaics for powering the robot and a 180-nm node CMOS circuit with approximately 1000 transistors to control the robot. The legs of the robot consist of surface electrochemical actuators (SEAs), microactuators developed at Cornell made of ultrathin atomic layer deposition platinum that bend to micrometer-scale radii of curvature in response to small voltages in aqueous environments [1,2]. Rigid panels of SiO_2 on either side of the actuator restrict the bending direction of the SEA to form a hinge. At the top and bottom of the robot are large, exposed platinum ground pads that serve as the counter electrodes to the actuators. Figure 1B shows a microscope image of the circuit of a released robot. Using infrared light and viewing a released robot from underneath, we can see parts of the CMOS circuit that controls the robot (Figure 1B). We fabricate many robots in parallel — Figure 1C shows an array of microscopic robots with a variety of designs prior to release. Each robot is inside a 300 μm by 300 μm square, meaning that almost 100,000 robots could be fabricated on a 4-inch wafer.

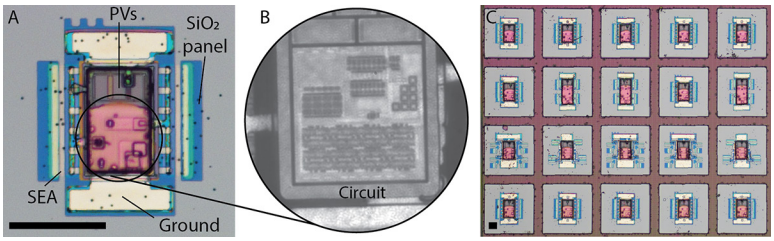

Figure 1: (A) Optical micrograph of a smart microscopic robot. (B) Infrared microscope image of a released microscopic robot showing the onboard CMOS circuit. (C) Optical micrograph of an array of microscopic robots. They are photolithographically fabricated in parallel on a silicon-on-insulator wafer. Scale bars are 100 μm.

Figure 2 shows an optical image of the circuit that controls the robot. This circuit is designed at Cornell and fabricated by X-FAB Silicon Foundries with a 180 nm node CMOS process on silicon-on-insulator (SOI) wafers. It has a simple function: to output phase-shifted square waves to the legs of the robot, allowing it to walk. We set the gait of the robot by wiring the legs of the robot to square wave outputs on the circuit with different phases. We set the frequency of the square wave outputs by wiring the I-shaped pins to the bar above them during post-processing, with frequencies ranging from about 1 Hz to about 128 Hz by factors of two.

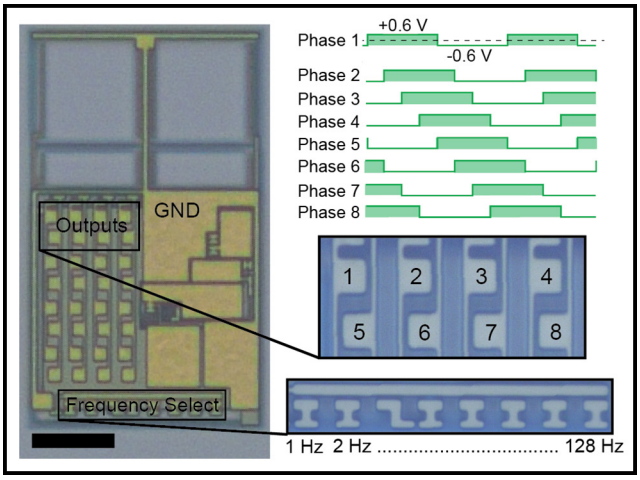

Figure 2: Optical micrograph of clockbot's integrated circuit showing the output pins for the eight phase-shifted square waves and the pins for selecting the output wave frequency. Scale bar is 20 µm.

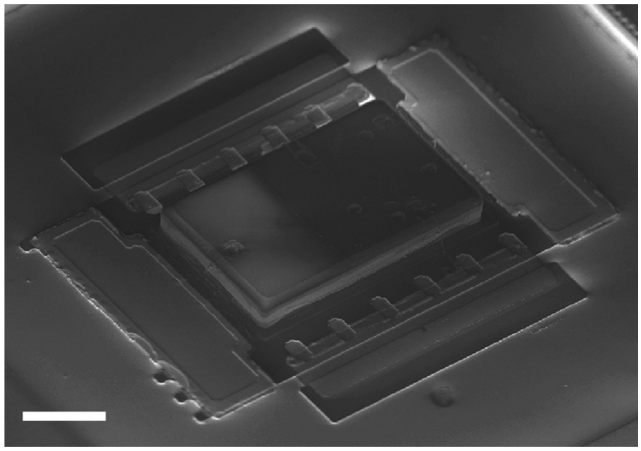

Figure 3: A scanning electron microscope image of a completed microscopic robot. The body of the robot, containing the photovoltaics and circuit, is about 15 µm tall. Scale bar is 30 µm.

After receiving the circuits from X-FAB, we perform post-processing on them to etch out the body (circuit and PVs) of the robot, create wires out from the circuit, shield the circuit from light, build legs and connect them to the circuit, and release the robots from the silicon substrate. This process is based on a variety fabrication protocols developed in our group [1-3], requires 13 layers of photolithography, and makes use of more than twenty CNF tools. A scanning electron microscope image of a completed robot is shown in Figure 3. This image shows the large topography resulting from etching out the body of the robot, about 15 μm tall. This creates several challenges during the fabrication process, requiring us to use the spray coater on the Gamma automatic coat-develop tool to coat the large vertical features completely with photoresist.

Upon completion of the fabrication process, we undercut the silicon beneath the robot and release it into an aqueous environment. Figure 4A shows a 3D model of a released robot. Upon release, the legs bend under the body of the robot. When we illuminate the robot with light, the robot moves autonomously without any additional inputs. Its design is inspired by the Purcell three-link swimmer [4]; instead of swimming, this robot walks by alternately moving its front and back legs. These robots operate in light intensities of about 1 kW/m^2, equivalent to direct sunlight outside on a sunny day. Figure 4B shows time-lapse images of a clockbot walking, with images taken at 25 s intervals.

Conclusions and Future Steps:

The robots shown here are only the beginning for CMOS-integrated smart microscopic robots. We are currently pursuing work on faster robots with more legs and more complex gaits and robots that respond to commands or following light gradients. Future designs will include robots with alternate propulsion mechanisms, additional sensors, and ways to communicate with each other and the outside world. As smart microscopic robots increase in complexity and capability, they have incredible potential for positive impact in numerous fields, from studying emergent behaviors in swarms of smart particles to performing medical procedures at the micron-scale.

References:

[1] Miskin, M. Z., et al. Electronically integrated, mass-manufactured, microscopic robots. Nature 584, 557-561 (2020).

[2] Liu, Q., et al. Micrometer-sized electrically programmable shape-memory actuators for low-power microrobotics. Science Robotics 6, (2021).

[3] Cortese, A. J., et al. Microscopic sensors using optical wireless integrated circuits. PNAS 117, 9173-9179 (2020).

[4] Purcell, E. M. Life at low Reynolds number. American Journal of Physics 45, 3-11 (1977).

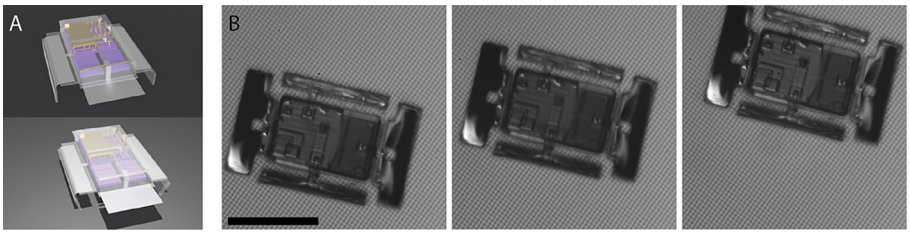

Figure 4: (A) Schematic of a CMOS integrated microscopic robot. The robot moves autonomously when powered by light. (B) A released microscopic robot walking on a glass substrate. Scale bar is 100 µm.

Characterizing Disjoining Pressure of Water in SiO_2 Nanochannels by Wicking Experiments

CNF Project Number: 2123-12

Principal Investigator(s): Shalabh C. Maroo

User(s): An Zou, Durgesh Ranjan

Affiliation(s): Department of Mechanical and Aerospace Engineering, Syracuse University, Syracuse, NY 13244

Primary Source(s) of Research Funding: National Science Foundation Career Award NO. 1454450; Office of Naval Research Grant NO. N000141812357

Contact(s): scmaroo@syr.edu, azou@syr.edu, dranjan@syr.edu

Website: http://maroo.syr.edu

Primary CNF Tools Used: Heidelberg mask writer - DWL2000, manual photoresist spinner, Gamma coat-develop tool, GCA auto stepper, ASML stepper, YES image reversal oven, ABM contact aligner, SÜSS MA6-BA6 contact aligner, e-beam evaporator, Oxford PECVD, GSI PECVD, Glen 1000 Plasma, Anatech resist strip, Oxford 81/82/100 etchers, P-T deep silicon etcher, Unaxis 770 deep silicon etcher, optical microscope, SEM, AFM

Abstract:

We characterized disjoining pressure of water in SiO_2 nanochannels by studying water wicking in 59 nm channels. The wicking in nanochannels was dominated by disjoining pressure. Wicking distance is proportional to square root of time, and the slope can be used to calculate the disjoining pressure, which can be as high as ~ 1.5 MPa in 59 nm channel. The work reported here is part of an article that is currently under review [1].

MECHANICAL DEVICES

Summary of Research:

The pressure in a thin liquid film, with thicknesses ranged from a few nanometers to hundreds of nanometers, differs from its bulk due to the considerable, if not dominant, intermolecular interactions. This pressure difference is characterized by disjoining pressure, which plays a fundamental role in a wide range of engineering and natural systems involving bubbles, foams, emulsions, and membrane, etc. Since disjoining pressure is originated from intermolecular interactions, it is significantly affected by the material of surrounding surfaces, which could be any combination of solid, liquid, and vapor. Although disjoining pressure in a non-polar liquid film has been well understood, comprehensive knowledge for polar liquids, like water on a silicon dioxide (SiO_2) surface, is still lacking. Here, we report an experimental characterization of disjoining pressure of water in 1D SiO_2 nanochannels (height: 59 nm) with all walls made of SiO_2, by studying the water wicking process in nanochannels.

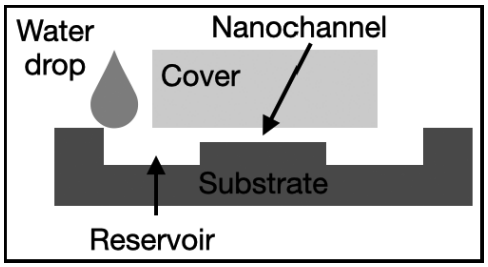

Figure 1: Sketch of cross-sectional view of the sample.

Figure 1 shows a cross-sectional view sketch of the nanochannel sample. The nanochannels, between two reservoirs, are ~ 2 cm long, 10 μm wide with 10 μm spacing between two adjacent channels. The channel height is 59 nm. The nanochannels were closed by bonding two wafers together. The fabrication process started from a silicon (Si) wafer — then ~ 3 μm thick photoresist (PR) was spin-coated and patterned through a standard photolithography process. The wafer was etched down for a certain depth to form open nanochannels, using patterned PR as mask. After removing the remaining PR, ~ 1 μm thick SiO_2 film was deposited using plasma enhanced chemical vapor deposition (PECVD), and was patterned by standard photolithography followed by dry etching, to serve as the hard mask for deep Si etching (Bosch process) for reservoirs (~ 30 μm deep). Then, after removing the remaining PECVD SiO_2 film using buffered oxide etchant, a new 300 nm thick PECVD SiO_2 film was deposited prior to bonding. The nanochannels were closed by bonding a glass piece above the channels using standard anodic bonding. The image from atomic force microscope (AFM) showing channel profile prior bonding was shown in Figure 2.

To perform wicking experiments, the sample was cleaned using deionized (DI) water, followed by oxygen plasma cleaning for 30 min. A DI water drop was placed in the reservoir, and water would wick into the channels, flow forward to fill the channel until reaching the other end. This wicking process was recorded using high speed camera

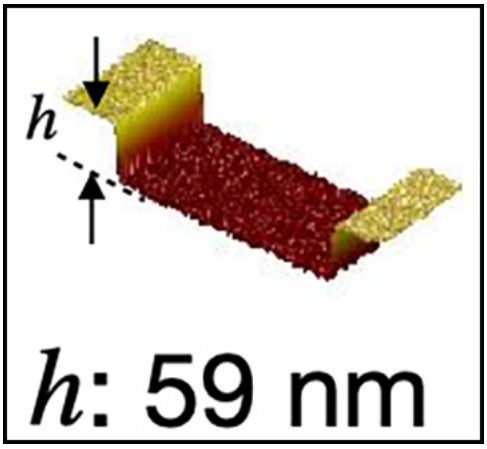

Figure 2: AFM image of channel profile prior bonding.

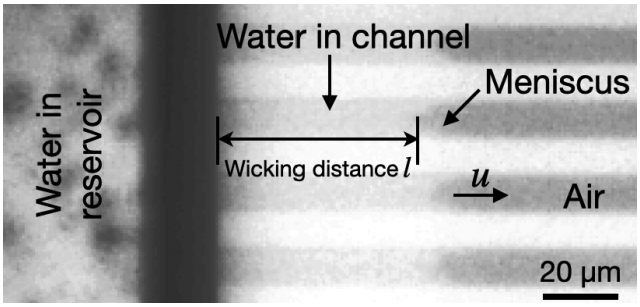

Figure 3: A typical image of the wicking from high speed video.

from the top. From the obtained video, the wicking distance l can be obtained by measuring the distance between the entrance and the position of the meniscus. Figure 3 shows a typical high speed image of the wicking. After finishing one test, the sample was heated to ~ 200°C on a hot plate in the open air to dry, which would take several minutes up to several hours. The wicking experiments for each sample were conducted at least four times to ensure repeatability.

The wicking distance (l) is proportional to square root of wicking time ($t^{1/2}$), as predicted by the simplified analytical solution (Eq. 1) of Navier-Stokes equation for wicking in a low specific ratio (height << width) rectangular cross-sectional channel [2].

$$l = \sqrt{\frac{h^2 \Delta P}{6\mu}} \cdot t^{1/2} = C \cdot t^{1/2}$$

where h is the channel height; ΔP is the total pressure difference driving the wicking; and μ is the fluid dynamic viscosity.

Figure 4 shows experimental results for both 59 nm and 1015 nm channels. As expected, the wicking distance is linear to square root of time with a slope C of 1.00 mm/s$^{1/2}$. As shown in Eq. 1, this slope is a function of channel geometry (height), liquid property (viscosity), and

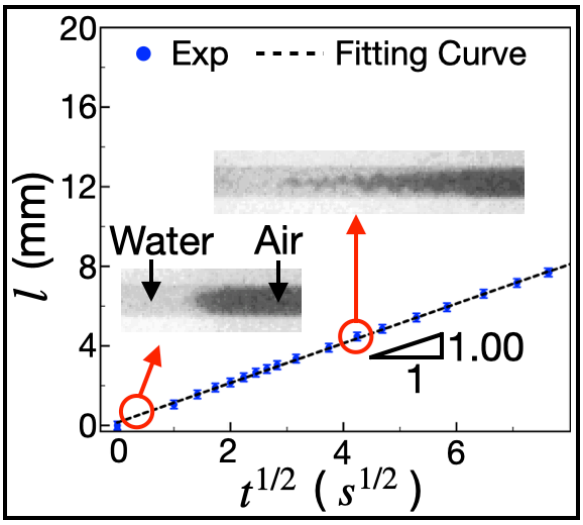

Figure 4: Variation of wicking distance with square root of time.

pressure difference. As both channel height and viscosity are known, the pressure difference can be calculated from experimentally obtained slope.

There are two potential contributions to the total pressure difference driving the wicking: disjoining pressure (due to the intermolecular interactions) and capillary pressure (due to the curvature of the meniscus). An interesting observation of wicking in 59 nm channels is that two types of meniscus were observed: regular-curved shape and wedge shape (Figure 4). The regular-curved meniscus occurred only within the first few hundreds of microns from the entrance. Beyond this initial distance, water was seen to flow much faster at the corners, forming the wedge-shape meniscus, which also led to air or vapor being momentarily trapped within the wicking liquid front. The different meniscus shape implies varied capillary pressure, however, constant slope C was observed during entire wicking process. Thus, capillary pressure was not major contribution to the total pressure difference; while disjoining pressure drove the wicking. With the estimation of capillary pressure in Ref. [1] and Eq. 1, disjoining pressure was calculated as 1.51 MPa. This is a first experimental characterization of disjoining pressure of water in SiO_2 nanochannels.

Conclusions and Future Steps:

We studied the water wicking in SiO_2 nanochannels, from which the disjoining pressure was characterized as 1.51 MPa in 59 nm channels.

References:

[1] A. Zou, S. Poudel, S.C. Maroo, arXiv preprint arXiv:2010.09928 (2020).

[2] B. E. Rapp, Microfluidics: Modelling, Mechanics and Mathematics. Micro and Nano Technologies, Oxford: Elsevier, 2017.

Origami-Inspired Micro-Robotic Arm

CNF Project Number: 2416-16

Principal Investigator(s): Itai Cohen

User(s): Baris Bircan

Affiliation(s): School of Applied and Engineering Physics, Laboratory of Atomic and Solid-State Physics, Kavli Institute at Cornell for Nanoscale Science; Cornell University

Primary Source(s) of Research Funding: National Science Foundation, Contract DMR-1719875; Army Research Office, Contract W911NF-18-1-0032

Contact(s): itai.cohen@cornell.edu, bb625@cornell.edu

Primary CNF Tools Used: Arradiance ALD Gemstar-6, Oxford ALD FlexAL, Oxford PlasmaLab 80+ reactive ion etchers, ABM contact aligner, AJA sputter deposition, AJA ion mill, Heidelberg mask writer - DWL2000

Abstract:

Origami, the Japanese art of paper folding, has recently found use in various engineering applications, leading to the development of origami-inspired systems ranging from the macro to the microscale. At and below the microscale, origami-inspired designs have allowed the use of planar lithographic fabrication methods to build systems that can self-fold into complex three-dimensional (3D) geometries. In our work, we make use of origami design principles to create a microscale robotic arm, which can be fabricated in large numbers using standard lithographic techniques. We envision that these devices will find uses in lab-on-a-chip devices, tissue manipulation and minimally invasive surgery.

Summary of Research:

Our group has previously demonstrated an approach capable of creating complex self-folding microsystems based on atomic layer deposition (ALD) nanofilms [1]. The method we have developed automatically generates photomasks for arbitrarily complex origami-inspired designs, which can then be used to fabricate self-folding microdevices based on ultra-thin ALD films.

One application being pursued with this approach is a microscale robotic arm based on ultra-thin, ALD based surface electrochemical actuators (SEAs) [2,3]. SEAs, which consist of 7.5 nm of platinum, deposited using the Arradiance ALD Gemstar-6, and a 2 nm thick titanium capping layer, deposited using the AJA sputter deposition system, operate in electrolyte and can bend down to several micron scale radii of curvature in response to electrical signals.

To microfabricate our design for the origami-inspired robotic arm (Figure 1A-B), we generate photomasks suitable for SEAs (Figure 2). Our design for the micro-robotic arm incorporates the origami-inspired surgical forceps (Oriceps) [4] as the gripping element, and includes folding hinges to generate translation and tilt, resulting in a total of three degrees of freedom. The leftmost photomask pattern shown in Figure 2 defines the regions that will be used to create upward bending, while the photomask pattern shown in the middle defines the regions that will be used to create downward bending. The rightmost photomask pattern defines the rigid, flat panels that will be used to restrict bending. These patterns are generated as BMP files and imported into L-Edit to create the full mask layout, which is then used to fabricate photomasks with the Heidelberg mask writer - DWL2000.

Figure 3 shows the first prototypes for our origami-inspired micro-robotic arm design, which include three electrodes to address the translation, tilt, and gripping degrees of freedom, and thin, isolated strips of platinum to carry applied electrical signals throughout the device. The three electrodes are permanently bonded to the substrate, which makes the devices semi-tethered. After the devices are released by wet etching the underlying Al release layer, the electrodes make it possible to apply driving voltages by making contact with a Pt/Ir micromanipulator probe.

We envision that the microscale manipulation capabilities offered by this SEA-based, origami-inspired micro-robotic arm will find uses in lab-on-a-chip devices, tissue manipulation and minimally invasive surgery.

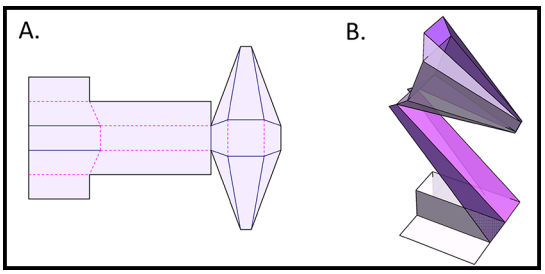

Figure 1: (A) Fold pattern and (B) 3D model for our origami-inspired robotic arm design, which incorporates the Oriceps [4] as the gripping element, and includes folding hinges to generate translation and tilt.

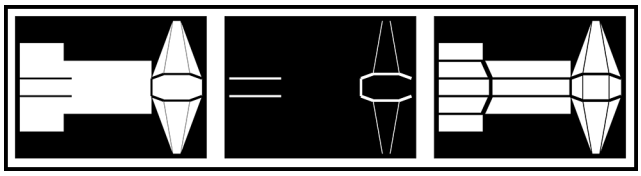

Figure 2: Photomask patterns used in fabrication of the micro-robotic arm design. The leftmost photomask defines the regions that will be used to create upward bending, while the photomask shown in the middle defines the regions that will be used to create downward bending. The rightmost photomask defines the rigid, flat panels that will be used to restrict bending.

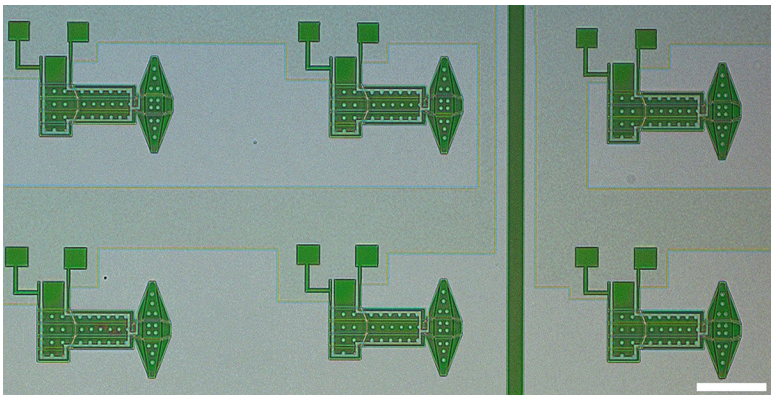

Figure 3: An array of microscale robotic arm devices prior to release. Each device is attached to three fixed electrodes that address the translation, tilt, and gripping degrees of freedom. Scale bar is 200 µm.

References:

[1] Bircan, B., Miskin, M. Z., Lang, R. J., Cao, M. C., Dorsey, K. J., Salim, M. G., Wang, W., Muller, D. A., McEuen P. L., and Cohen, I., "Bidirectional self-folding with atomic layer deposition nanofilms for microscale origami," Nano Letters, vol. 20, no. 7, pp. 4850-4856, 2020.

[2] Miskin, M. Z., Cortese, A. J. Cortese, Dorsey, K., Esposito, E. P., Reynolds, M. F., Liu, Q., Cao, M., Muller, D. A., McEuen, P. L., Cohen, I., "Electronically integrated, mass-manufactured, microscopic robots," Nature, vol. 584, no. 7822, pp. 557-561, 2020.

[3] Liu, Q., Wang, W., Reynolds, M. F., Cao, M.C., Miskin, M.Z., Arias, T.A., Muller, D.A., McEuen, P.L., and Cohen, I., 2021. Micrometer-sized electrically programmable shape-memory actuators for low-power microrobotics. Science Robotics, 6(52), 2020.

[4] Edmondson, B. J., Bowen, L. A., Grames, C. L., Magleby, S. P., Howell, L. L., Bateman, T. C., "Oriceps: Origami-inspired forceps," in ASME 2013 conference on smart materials, adaptive structures and intelligent systems, American Society of Mechanical Engineers Digital Collection, 2013.

Electrically Controllable Micro-Machines

CNF Project Number: 2416-16

Principal Investigator(s): Itai Cohen, Paul L. McEuen

User(s): Qingkun Liu, Wei Wang, Jacob Thomas Pelster, Hanyu Alice Zhang

Affiliation(s): Kavli Institute at Cornell for Nanoscale Science, School of Applied and Engineering Physics, Laboratory of Atomic and Solid-State Physics, Department of Physics; Cornell University

Primary Source(s) of Research Funding: National Science Foundation, Contract DMR-1719875; DMR-1435829 Army Research Office, Contract W911NF-18-1-0032

Contact(s): itai.cohen@cornell.edu, plm23@cornell.edu, ql59@cornell.edu, ww459@cornell.edu, jtp246@cornell.edu, hz496@cornell.edu

Primary CNF Tools Used: Oxford ALD FlexAL, Arradiance ALD Gemstar-6, Oxford 81/100 etchers, ABM contact aligner, CVC SC4500 odd-hour, AJA sputter deposition, AJA ion mill, Oxford Cobra ICP etcher, Heidelberg DWL2000

Abstract:

Electromechanically adaptive materials are poised to revolutionize microscopic robots, robotic materials, and bio-implantable devices. Previously, we have demonstrated that the electrochemical micro-actuators made by atomically thin layers of metals and dielectrics could bend in response to a low voltage of ~ 1V. Here, we utilized this new type of micro-actuators to develop complex microstructures and micromachines, such as auxetic mechanical metamaterials, neural probes, and artificial cilia.

Summary of Research:

Nanofabrication of electromechanically active materials could create micromachines with unparalleled properties and functionalities [1]. The core of these devices consists of a nanometer-thin platinum layer as an electrochemically active material capped on one side by titanium as an inert layer. To demonstrate their broad applications, our team has developed three types of such micro-devices: auxetic mechanical metamaterials, neural probes, and artificial cilia.

Our team first developed micro-sized auxetic mechanical metamaterials by using origami design principles [2]. Auxetic mechanical metamaterials comprised of rigid panels that can locally splay, have the ability to yield reconfigurable curved surfaces and generate different locomotion gaits for robotics applications. We show that such electrically actuated auxetic metamaterials can be utilized to design micro-scale robots. As in their macroscopic counterparts, the expansions and contractions in our devices are achieved by splaying neighboring panels. To achieve this splay actuation we developed an origami hinge based on a single mountain and two valley folds. The actuation of the hinges is controlled by applying voltage to a nm thin surface electrochemical actuator. The local expansions and contractions alter the local Gaussian curvature of the metamaterial sheet allowing it to reconfigure into a continuous set of three-dimensional shapes. We modeled the target shapes using a reversed design approach in which the shapes are iterated towards target shapes by selecting optimal actuations of the splay hinges. We then show experimentally we are able to generate 2D and 3D shapes by actuating the hinges. Based on these proof of principle results, we are working towards manufacturing untethered metamaterial-based micro-scale robots with integrated photovoltaics and timing circuits that control the sequence of hinge actuations and resulting global shapes and locomotion gaits.

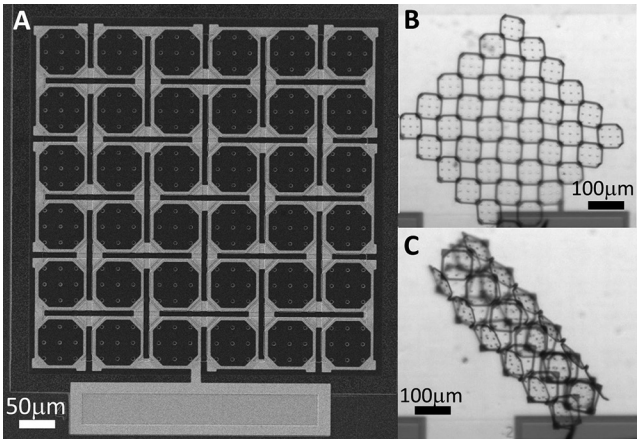

Figure 1: Electrically programmable auxetic mechanical metamaterials. (A) SEM image of a mechanical metamaterial sheet. (B,C) The sheet could deform into two-dimensional and three-dimensional shapes.

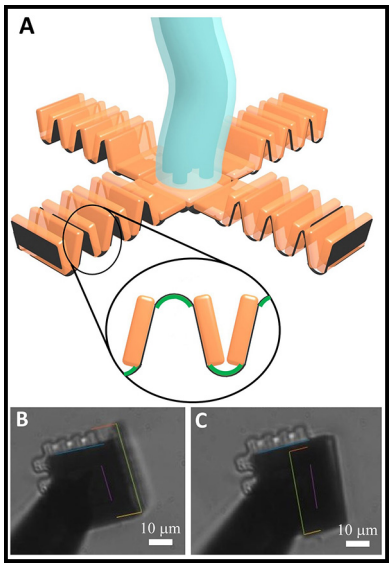

Figure 2: Robotic neural probe. (A) Schematic of an origami-based deployable neural probe. (B,C) Optical images of the bendable probe actuated from -88° to 134° when varying the voltage from 0.6V to -1.2V in phosphate buffer solution.

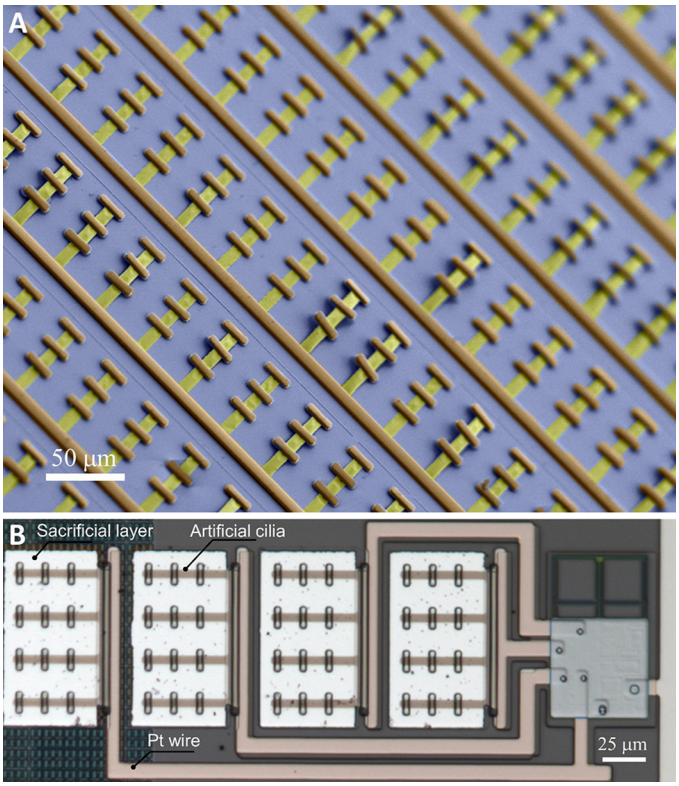

Figure 3: Electrically actuated artificial cilia. (A) SEM image of artificial cilia arrays. (B) Optical image of artificial cilia integrated with control circuit.

Our second project is to use the micro-actuator and origami principle to design robotic neural probes. The ability to actuate the non-toxic materials in the brain paves the way for neural sensing probes that do not require an invasive borehole the size of the area to be sensed, through the cranium and pia-mater. Although the platinum-based micro-actuator we developed previously works perfectly in PBS solution, the fact that the oxidization reaction that drives the actuation of platinum is not scalable with the thickness of the platinum, meaning only the same amount of strain energy can be held in a platinum beam regardless of the thickness (implying a smaller curvature). This limitation presents a challenge with the group's current actuation design if used for neural probes. Since the brain, or brain-like gel, requires much more force to move through compared to the aqueous solution currently used by the group, an actuator needs to store enough energy to effectively displace a gel, while still being able to actuate over a wide range of angles. For this reason, we explored bulk electrochemical micro-actuators that utilize hydrogen adsorption/desorption effect to generate the strain in the thin film. In this system, hydrogen diffuses into the bulk of actuator, creating a bulk stress in the composite that scales with the thickness of the actuator. This new type of micro-actuator has much larger output force than the preview platinum micro-actuator while keeping the bending radius as small as the platinum counterpart.

Last, our team designed microfluidic devices that comprise arrays of such micro-actuators [3]. Microfluidic patterns are crucial in aspects from regulating cerebrospinal fluid in brain, guiding chemical reactions to manipulating particles. The traditional microfluidic devices use micro-channels and external pumps to guide the flow motion. The flow direction is determined by the micro-valves and cannot be changed once fabricated. Here, a new type of integrated microfluidic manipulation system which is built on the electrically actuated artificial cilia is proposed to achieve reprogrammable flow motions. The electrical chemical platinum actuator which has low voltage, low power and fast response time is used to fabricate the artificial cilia. The artificial cilia are compatible with CMOS fabrication and packaging technology and can be easily manipulated by computer software and micro-processor through tethered or untethered control. It gives a new platform to make powerful microfluidic devices and study the programmable motion of micro robotics.

References:

[1] Liu, Q., Wang, W., Reynolds, M.F., Cao, M.C., Miskin, M.Z., Arias, T.A., Muller, D.A., McEuen, P.L. and Cohen, I., 2021. Micrometer-sized electrically programmable shape-memory actuators for low-power microrobotics. Science Robotics, 6(52), 2020.

[2] Liu, Q., Wang, W., Sinhmar, H., Cortese, A., Griniasty, I., Reynolds, M., Taghavi, M., Apsel, A., Kress-Gazit, H., McEuen, P. and Cohen, I., Electrically Programmable Micro-scale Morphing Robots Based on Mechanical Metamaterials. Bulletin of the APS 2021.

[3] Wang, W., Liu, Q., Reynolds, M., Miskin, M., McEuen, P. and Cohen, I., 2021. Electrically actuated artificial cilia for microfluidic applications. Bulletin of the American Physical Society, 2021.

Nanoscale Hot-Wire Anemometer Probe with Contoured Silicon Probe Body

CNF Project Number: 2532-17

Principal Investigator(s): Gregory P. Bewley

User(s): Edmund T. Liu

Affiliation(s): The Sibley School of Mechanical and Aerospace Engineering, Cornell University

Primary Source(s) of Research Funding: The Sibley School of Mechanical and Aerospace Engineering, Cornell University

Contact(s): GPB1@cornell.edu, ETL46@cornell.edu

Primary CNF Tools Used: Heidelberg mask writer - DWL2000, SÜSS MA-6, Oxford PECVD, CVC SC4500 odd-hour evaporator, Oxford 82, Plasma-Therm Versaline deep silicon etcher, Unaxis 770 deep silicon etcher

Abstract:

Turbulence measurements are difficult to take due to the large separation of scales present in a flow. At the smallest scales, where conventional probes are limited by spatial and temporal resolution, measurements are a result of the physical dimensions and thermal mass of the sensing element. Semiconductor fabrication equipment enables the manufacturing of hot-wires much smaller than their conventional counterparts in volume, driving down costs while increasing measurement sensitivity. We report on the successful creation of such a probe with a sensing element measuring 60 × 2 × 0.1 μm supported by a contoured silicon body. The probe is compared to a conventional probe 1.27 μm in diameter in jet turbulence generated by a calibration tank and exhibits higher temporal resolution. The high-throughput process is found to have a yield rate > 95%.

Summary of Research:

Hot-wire anemometry is a method to measure flow velocities and is commonly used for turbulent flows due to high frequency response, spatial resolution, and ease of use. Hot-wires operate by heating up a small wire with electrical current. Placed in a flow, generated heat is convected from the wire to the fluid, with higher flow velocities corresponding to greater amounts of heat convection. By exploiting the wire material's temperature-dependent resistance, the measured voltage across the wire is correlated to the flow velocity.

Sensor performance is significantly impacted by the physical dimensions and material of the wire. Smaller wires exhibit high frequency response due to a small thermal mass, and shorter lengths lead to less spatial filtering. Moreover, a large length-to-diameter ratio is desired to mitigate the effects of end-conduction, where generated heat is conducted to the wire supports, rather than convected to the flow of interest. The smallest conventional wires available measure 0.6 to 1.27 μm in diameter and require labor-intensive soldering and chemical etching, thereby limiting probe throughput. Semiconductor manufacturing equipment is promising because it allows for the fabrication of sensing elements unachievable by conventional means at high-throughput and repeatability. On a single 4-inch wafer, hundreds of such probes may be created.

Initial work on hot-wire probes manufactured with semiconductor processing equipment was performed at Princeton University, resulting in the development of the nanoscale thermal anemometry probe (NSTAP) [1]. Unlike the sharp features used in the NSTAP, we designed a contoured metal film and probe body using AutoCAD and MATLAB. Original NSTAP processes relied on deep reactive-ion etching (RIE) and exploited RIE-lag to produce a 3D aerodynamic probe body. A similar process is used to create in-house probes.

First, 500 nm and 4 μm of silane-based silicon dioxide is formed through plasma-enhanced chemical vapor deposition (PECVD) on either side of a double-side polished wafer with the Oxford PECVD. 100 nm of platinum with a 10 nm titanium adhesion layer is then evaporated onto the 500 nm oxide and lifted off with a LOR bi-layer exposed with the SÜSS MA-6 contact aligner. On the backside, a fine pattern consisting of trenches used to induce RIE-lag is transferred from a SPR220-3.0 photoresist softmask to the 4 μm oxide to form a hardmask. Softmask exposure is performed with the MA-6 in vacuum contact mode, and the hardmask is etched with the Oxford PlasmaLab 82. Through-wafer etching is then performed with both the Plasma-Therm VersaLine and the Unaxis 770 deep silicon etchers, and the profile is smoothed with isotropic silicon etching. Finally, the remaining 500 nm oxide layer is etched to release the probes and free-standing platinum wire.

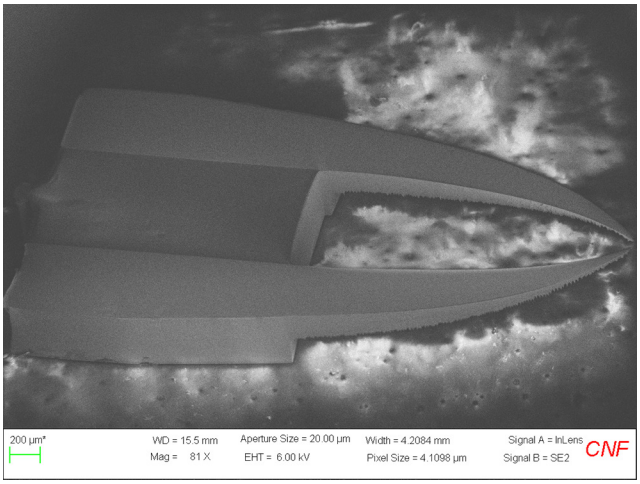

Figure 1: Probe following release from the wafer. The platinum trace and supporting silicon body are contoured, and the three-dimensional taper, a result of RIE-lag, is visible.

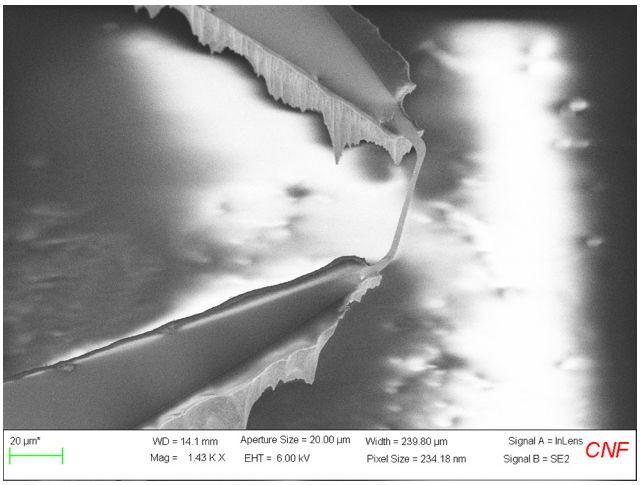

Figure 2: Magnified SEM image of the thin free-standing platinum wire.

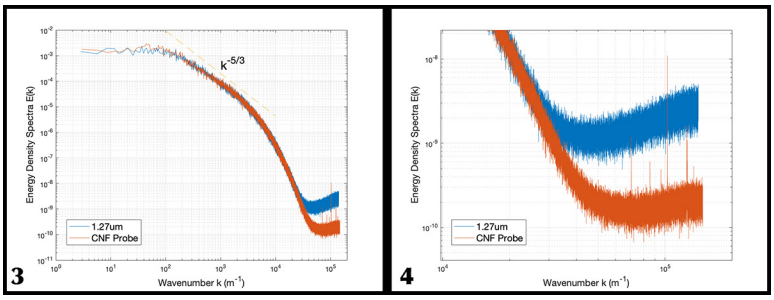

Figure 3, left: Comparison of turbulent spectra from a jet measured with a CNF probe and conventional 1.27 µm hot-wire. We observe a high degree of agreement in the collected spectra. Figure 4, right: Magnified image of the high-frequency spectra. Compared to the conventional hot-wire, the CNF probe is able to resolve more of the dissipation range. The spectra appear to flatten at higher frequencies, most likely due to the noise floor of external electronics.

Figures 1 and 2 show the final probe following release from the wafer and a magnified image of the free-standing wire, respectively. The tapered profile created using RIE-lag is visible and extends downstream from the wire, where there is minimal supporting silicon. The probe is verified using jet turbulence produced by a calibration tank. Placed about twelve opening diameters away from the jet outlet, the probe successfully measures a turbulent spectra, with high agreement with a conventional 1.27 μm hot-wire as shown in Figure 3.

Looking more closely at the high-frequency components of the spectra, we see that the microfabricated probe resolves even more of the dissipation range.

References:

[1] Vallikivi M. and Smits A.J., "Fabrication and Characterization of a Novel Nanoscale Thermal Anemometry Probe," Journal of Microelectromechanical Systems, vol. 23, no. 4, pp. 899-907, Aug. 2014, doi: 10.1109/JMEMS.2014.2299276.

Hot-Wire Anemometer Probe with SU-8 Support Structure

CNF Project Number: 2532-17

Principal Investigator(s): Gregory P. Bewley

User(s): Edmund T. Liu

Affiliation(s): The Sibley School of Mechanical and Aerospace Engineering, Cornell University

Primary Source(s) of Research Funding: The Sibley School of Mechanical and Aerospace Engineering, Cornell University

Contact(s): gpb1@cornell.edu, etl46@cornell.edu

Primary CNF Tools Used: Heidelberg mask writer - DWL2000, SÜSS MA-6, Oxford PECVD, CVC SC4500 odd-hour evaporator, SU-8 hot plates

Abstract:

Nanoscale hot-wire anemometer probe fabrication processes have focused largely on the micromachining of silicon substrates to form support structures, an etch-heavy procedure. We detail the development of a hot-wire probe constructed through additive means with SU-8. An additive approach to manufacturing holds a number of advantages over silicon etching, including the ability to precisely define the probe structure with photolithography and control the final thickness of the supports.

Summary of Research:

Significant benefits in the sensing capabilities of hot-wire anemometer probes, including improved temporal and spatial resolutions, may be achieved by shrinking physical wire dimensions. Semiconductor manufacturing tools are well-suited to this task, allowing for the fabrication of wires measuring only tens of microns in length, microns in width, and hundreds of nanometers thick, previously unachievable or impractical with conventional means. Existing hot-wire probes created through such means rely on silicon etching to produce the probe support structures, utilizing deep reaction-ion etching (RIE) and RIE-lag effects to produce a 3D aerodynamic structure.

Etched silicon structures are the result of subtractive processes, where the substrate is meticulously sculpted and forms an integral component of the final sensor. Associated processes are proven and have resulted in successful probe fabrication at high yield and throughput. However, it is found that the final probe outline after etching seldom resembles the original mask design, and the process requires multiple design iterations to achieve a desired shape. Moreover, due to the thin silicon supports near the wire and the lack of an etch stop, the process is sensitive to over-etching that may undercut and thus jeopardize the sensor.

To address these issues, additive processes are used instead. Rather than using the substrate as a support material, structures are built upon a silicon wafer and subsequently lifted off. By using SU-8, a negative photoresist with a wide range of possible thicknesses, the final probe shape may be precisely defined by light, avoiding an iterative design process. SU-8 also allows for control over the final thickness of the supports by using formulations with different viscosities and modifying spin parameters.

SU-8 probes are manufactured by first depositing a 500 nm silicon dioxide film on a single-side polished silicon wafer using plasma-enhanced chemical vapor deposition (PECVD). This film acts as a sacrificial layer on which the probes lie. 100 nm of platinum with a 10 nm titanium adhesion layer is then evaporated and lifted off with a LOR bi-layer. Two SU-8 layers of varying thickness are processed. First, a layer of SU-8 2035 is spun to about 16 μm and soft-baked according to datasheet guidelines. Only the arms and solder pads of the evaporated metal trace, excluding the wire, are exposed. Next, a second layer of SU-8 2035 is spun on the exposed first layer and soft-baked, reaching a thickness of about 100 μm. This layer serves to hold both arms of the probe in fixed positions. After exposure of the second layer, a post-exposure bake (PEB) is performed at 55°C overnight. The low PEB temperature is used to minimize residual stress in the final SU-8 structure [1].

Finally, the probes are lifted from the wafer by immersion in concentrated 49% HF, which etches the PECVD oxide underneath each probe. Following lift-off, the probes are rinsed in water and dried in air.

A probe lifted from the substrate is displayed in Figure 1. The relatively thin probe arms and the thicker support structure are visible, as is the platinum wire. A prominent feature of the probe is the peeling of the metal film. Due to residual stresses during processing, the SU-8 will tend to

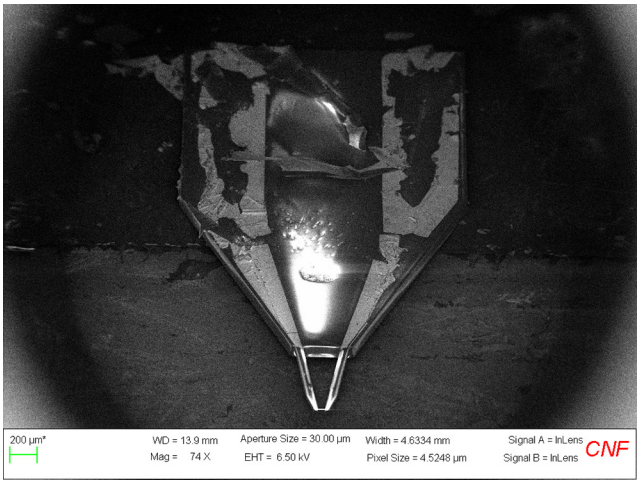

Figure 1: An SU-8 probe lifted from the substrate shows significant metal tearing, an effect of deflection of the SU-8 probe arms.

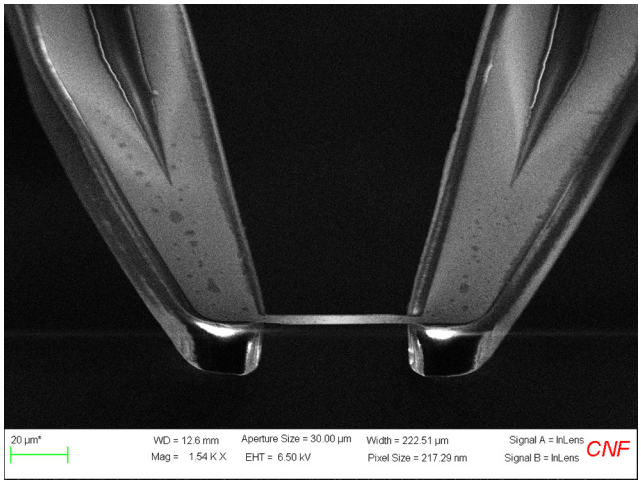

Figure 2: Magnified image of an SU-8 probe. The arm outline is precisely defined by photolithography and the thickness set by SU-8 processing parameters. Metal film peeling is visible along the center of the arms.

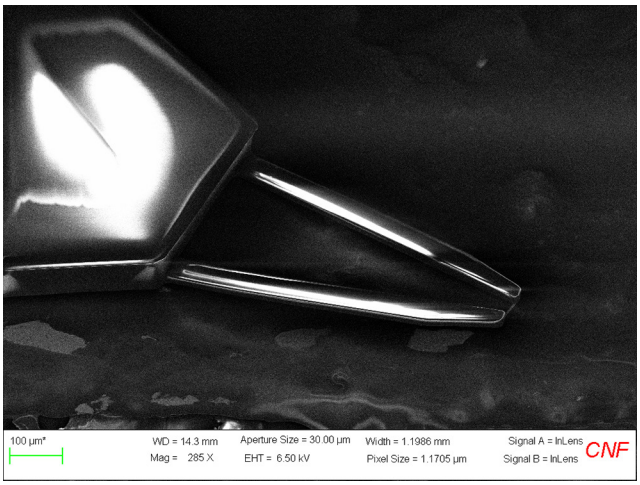

Figure 3: Backside of probe showing varying thickness of SU-8 layers.

deflect, pulling the metal film from the substrate and leading to tearing. This tearing is also visible along the probe arms in Figure 2. However, we see that the SU-8 arms are well-defined, with a controlled thickness. Figure 3 shows the underside of the probe, where the varying thickness of the SU-8 layers is clear.

Future work will focus on modifying the metal film stack and SU-8 processing to minimize stress and tearing.

References:

[1] Li B., Liu M. and Chen Q., "Low-stress ultra-thick SU-8 UV photolithography process for MEMS," J. Micro/Nanolith. MEMS MOEMS, vol. 4, no. 4, 043008, Oct. 2015, https://doi.org/10.1117/1.2117108.

Limit Cycle Oscillations in Silicon Structures Using Opto-Thermal Excitation

CNF Project Number: 2732-18

Principal Investigator(s): Prof. Alan Taylor Zehnder

User(s): Aditya Bhaskar

Affiliation(s): Sibley School of Mechanical and Aerospace Engineering, Cornell University

Primary Source(s) of Research Funding: National Science Foundation (NSF), United States, grant number CMMI-1634664

Contact(s): atz2@cornell.edu, ab2823@cornell.edu

Primary CNF Tools Used: Heidelberg mask writer - DWL2000, Hamatech hot piranha, DISCO dicing saw, GCA 6300 DSW 5x g-line wafer stepper, Unaxis 770 deep silicon etcher, Anatech plasma asher, Leica CPD300 critical point dryer, Zygo optical profilometer, Zeiss Supra SEM

Abstract:

Self-sustaining micro-oscillators may find applications in fields such as time-keeping and sensing, due to their high quality factors and frequency stability. This work involves the study of pairs of opto-thermally driven oscillators and their characteristics such as synchronization to each other and frequency entrainment to an external drive. The experimentally observed phenomena are complemented by theoretical and numerical studies.

Summary of Research:

Our work involves the study of the nonlinear characteristics of limit cycle oscillators (LCO's) and the emergence of synchronization in such systems. A limit cycle oscillator consists of a resonating element supplied by a constant energy source with a built-in positive feedback between the LCO's motion and the external energy source. Such active oscillations can be distinguished from a resonance response caused by an external periodic force applied to a passive resonating element [1].

We focus on single and pairs of clamped-clamped beam micro-resonators which were fabricated on a 0.75″ × 0.5″ silicon-on-insulator (SOI) chip with a 205 nm silicon device layer. The steps of general photolithography were followed with the exposure done on a GCA 5x g-line stepper.

After development, the silicon device layer was etched using the Bosch process. The devices were released using a buffered oxide etch (BOE) of the 400 nm silicon dioxide layer underneath followed by critical point drying. An image of the released devices taken using scanning electron microscopy (SEM) is shown Figure 1.

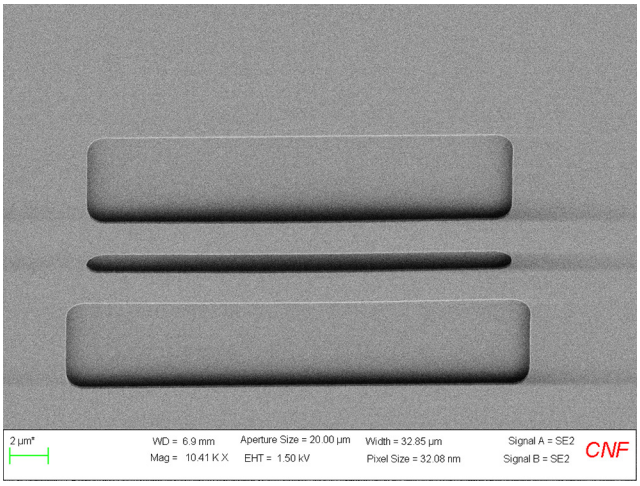

Figure 1: SEM image of clamped-clamped silicon beams fabricated from an SOI stack with 205 nm silicon device layer and 400 nm silicon dioxide.

The SOI chip with the micro-resonators is indium-bonded to a piezoelectric shaker housed in a vacuum chamber at a pressure of approximately 1e-7mBar. A continuous-wave laser beam with wavelength 633 nm is focused at the center of the microresonators, and part of the light is absorbed by the resonator, while part is transmitted and reflected back to it, thus setting up a Fabry-Perot interference cavity. The absorbed light causes the beam to undergo thermal expansion, which in turn modulates the amount of light absorbed. Thus, the microresonator undergoes self-sustaining limit cycle oscillation. The reflected laser beam modulated due to the oscillations is directed to a high-speed photodetector and its frequency content is recorded using a spectrum analyzer. The analyzer also serves a second purpose of providing the input signal to the piezoelectric shaker when an external inertial drive is required [2].

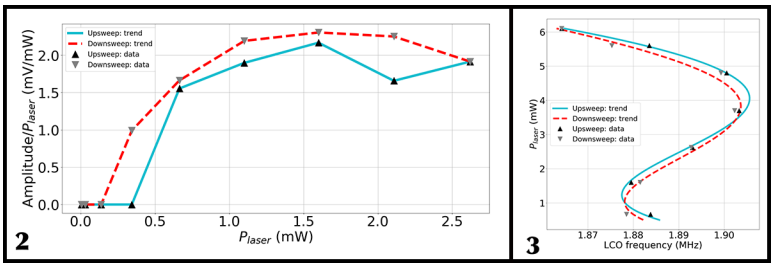

Figure 2, left: The birth of LCO in a Hopf bifurcation: variation of normalized signal amplitude with laser power upsweep and downsweep. Figure 3, right: Variation of the LCO frequency with laser power upsweep and downsweep.

From the resonance response it can be noted that the resonator exhibits spring softening, i.e. the frequency decreases with increasing amplitude of motion. The external drive amplitude is kept fixed and the frequency is swept up and down. The plateaus in the drive LCO curves correspond to entrainment regions. Hysteresis can again be noted in this experiment. It is expected that the frequency span for entrainment will become larger for higher drive amplitudes.

The appearance of a limit cycle response is shown in Figure 2. The laser is focused on a silicon beam 36 μm long and 2 μm wide and the laser power hitting the sample is swept up and then down. In the laser upsweep, we see that the LCO appears at around 0.3 mW of incident power and the signal amplitude normalized by the laser power is approximately constant. The transition to limit cycle is accompanied by a Hopf bifurcation [3], which is seen in numerical models for this system. The downsweep curve shows hysteretic behavior of the oscillator with laser power. For the same device, the frequency response of the LCO with laser power is shown in Figure 3. The response is non-monotonic with laser power. It is also noted that at low laser power the LCO's have greater frequency stability than at higher powers.

Frequency entrainment refers to the phenomenon of an external periodic driving force causing the frequency of the LCO to match that of the drive. The key parameters that determine entrainment of an LCO is the frequency detuning between the LCO and the external drive and the drive amplitude. Figure 4 shows the results of an entrainment experiment on a single LCO. The external drive is provided by the piezoelectric shaker and the swept frequency and amplitude are controlled by the spectrum analyzer [4]. The undriven LCO response and the resonance responses are plotted as a reference for the entrainment curves.

Conclusions and Future Steps:

Opto-thermally driven limit cycle oscillations are observed in the clamped-clamped silicon microresonators. They show other nonlinear behavior such as frequency entrainment to an external inertial drive. Further experiments will be conducted on pairs of beams coupled elastically via silicon bridges. Coupling between two frequency-detuned oscillators is expected to result in self-synchronization of the beams. Further parameter spaces such as coupling strength, frequency detuning between two LCO's, and the influence of the external drive will be explored.

References:

[1] Pikovsky, Arkady, et al. "Synchronization: a universal concept in nonlinear sciences." No. 12. Cambridge university press, 2003.

[2] Blocher, David. "Optically driven limit cycle oscillations in MEMS." (2012).

[3] Aubin, Keith, et al. "Limit cycle oscillations in CW laser-driven NEMS." Journal of microelectromechanical systems 13.6 (2004): 1018-1026.

[4] Blocher, David B., Alan T. Zehnder, and Richard H. Rand. "Entrainment of micromechanical limit cycle oscillators in the presence of frequency instability." Journal of Microelectromechanical Systems 22.4 (2013): 835-845.

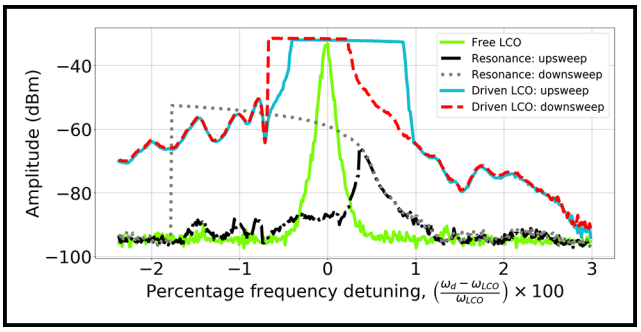

Figure 4: Frequency entrainment of an LCO by an external inertial drive on frequency upsweep and downsweep. The regions of entrainment correspond to the plateaus in the peak tracking signals. The free LCO response and resonance response on frequency upsweep and downsweep are also plotted for reference.